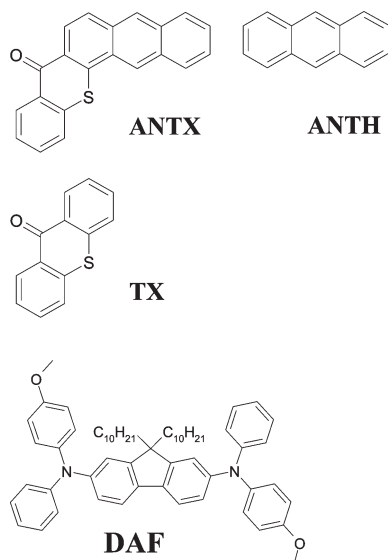


Scheme 1. Molecular Structures of Chromophores



derivatives.^{21–24} However, those Norrish II systems,²⁵ whose lowest excited triplet states (T_1) are efficient hydrogen abstractors, possess very low δ .²⁶ This low 2PA ability is connected to the presence of a weakly allowed transition with a $n\pi^*$ character in the lowest-energy band of the linear absorption spectrum.^{27–30} Reciprocally, the $n\pi^*$ nature of the T_1 state is mainly responsible for the high reactivity of these photoinitiators. As a consequence, increasing the dimensionality of the chromophore by extending the electronic delocalization should promote an increase in δ to the detriment of the photoreactivity due to a concomitant strengthening of the $\pi\pi^*$ character at the T_1 state. This photophysical paradox can be overcome through the use of a Förster type energy transfer (ET) mechanism.³¹ For instance, we recently developed an intramolecular energy transfer on the basis of a photoinitiator integrating a camphorquinone as an energy acceptor chromophore.³² The photoactivation of this highly reactive hydrogen abstractor was promoted by two-photon excitation of a diaminofluorene derivative used as an energy donor. We then demonstrated that our system exhibits a much higher two-photon initiating efficiency as the electron-rich diaminofluorene photoinitiator. Other methods were based on the relevant positioning of a ketone substituent in the organic structure so that the ketone displays a double role as a strong electron-withdrawing group, which is involved in the mechanism leading to the 2PA enhancement and as an efficient spin–orbit coupling agent promoting intersystem crossing to the triplet manifold.^{33–35} In the present paper, we adopt an equivalent strategy by integration of a thioxanthone system into a more conjugated chromophore (Scheme 1). As the reactivity of this photoinitiator family is mainly controlled by vibronic coupling between nearby $n\pi^*$ and $\pi\pi^*$ excited states,^{27–30,36–38} a chevron-shaped structure was privileged with respect to the linear one in order to prevent a total electronic delocalization, which should strongly stabilize the $\pi\pi^*$ level and reduce this requested vibronic coupling. A detailed linear and nonlinear spectroscopic analysis will be presented in connection with the one- and

two-photon induced polymerization properties of this new thioxanthone derivative.

2. EXPERIMENTAL SECTION

2.1. Materials. Thioxanthone (TX), anthracene (ANTH), thiosalicylic acid, and *N*-methyl diethanolamine (MDEA) were purchased from Aldrich. Polyethylene glycol diacrylate monomer (SR344, $M_w = 508 \text{ g mol}^{-1}$) was provided by Sartomer. SR344 is a difunctional oligoether acrylate that exhibits a low viscosity of 40 cps at 25 °C. A viscous difunctional monomer, Ebecryl 605, was purchased from Cytec. This monomer, which has a viscosity of 1000 cps at 25 °C, is a formulation based on bisphenol A epoxydiacrylate and tripropyleneglycol diacrylate (75/25 in weight). The solvents used for absorption and emission analysis are as follows: hexane (HEX), toluene (TOL), ethyl ether (EOE), butyl acetate (BTA), ethyl acetate (ETA), 2-methyl tetrahydrofuran (2-MTHF), tetrahydrofuran (THF), dichloromethane (CH_2Cl_2), dimethylformamide (DMF), acetonitrile (ACN), ethanol (EtOH), and methanol (MeOH). All the solvents employed were Aldrich or Fluka spectroscopic grade.

Synthesis of Naphto[2,3-*c*]thioxanthen-8-one (ANTX). Synthesis strategy of ANTX is similar to that reported in ref 39. Anthracene (1.0 g, 6 mmol) is dissolved into 30 mL of heated acetic acid. The solution is slowly added into thiosalicylic acid (0.3 g, 2 mmol) under stirring. Six milliliters of concentrated sulfuric acid is then added into the solution. The reaction mixture was refluxed for 4 h and then cooled to room temperature overnight. The mixture is carefully poured under stirring into 200 mL of boiling water and then maintained boiling during 5 min. The solution is cooled and filtered. The residue is washed with hot ethanol ($2 \times 50 \text{ mL}$). The precipitate is then recrystallized with chloroform. Yield (0.3 g, 50%).

$M_p = 254 \text{ }^\circ\text{C}$. $^1\text{H NMR}$ (CDCl_3) $\delta = 7.54\text{--}7.64$ (3H, m), 7.70 (1H, td, $J = 8.0 \text{ Hz}$, $J = 1.2 \text{ Hz}$), 7.79 (1H, d broad, $J = 7.2 \text{ Hz}$), 7.97 (1H, d, $J = 8.7 \text{ Hz}$), 8.05–8.10 (1H, m), 8.11–8.16 (1H, m), 8.48 (1H, s), 8.70 (1H, d, $J = 9.2 \text{ Hz}$), 8.69 (1H, dd, $J = 8.0 \text{ Hz}$, $J = 1.2 \text{ Hz}$), 9.0 (1H, s) ppm. $^{13}\text{C NMR}$ (CDCl_3) $\delta = 123.4, 123.7, 126.4, 126.5, 126.8, 127.0, 127.05$ (q), 127.3, 127.4, 127.4 (q), 127.9, 128.7, 129.4 (q), 129.5, 131.4 (q), 131.7 (q), 132.0, 133.4 (q), 135.8 (q), 138.4 (q), 179.8 (q) ppm. IR (KBr) ν_{max} : 683, 727, 743, 872, 894, 872, 1158, 1327, 1340, 1420, 1437, 1592, 1626, 3033, 3053 cm^{-1} . HRMS (APCI⁺): found $[\text{M}+\text{H}]^+$ 313.0690, calcd for $\text{C}_{21}\text{H}_{13}\text{OS}$ 313.0681.

9,9-Didecyl-*N*,*N'*-bis{4-methoxyphenyl}-*N*,*N'*-diphenyl-9H-fluorene-2,7-diamine (DAF). The synthesis and the characterization of DAF is described in refs 32 and 40.

2.2. General Techniques. Absorption measurements were carried out with a Perkin-Elmer Lambda 2 spectrometer. Steady-state fluorescence and phosphorescence spectra were collected from a FluoroMax-4 spectrofluorometer. Emission spectra are spectrally corrected, and fluorescence quantum yields include the correction due to solvent refractive index and were determined relative to quinine bisulfate in 0.05 N sulfuric acid ($\Phi = 0.52$).⁴¹

Phosphorescence and steady-state anisotropy measurements were performed in 2-methyl tetrahydrofuran at 77 K. The samples are placed in a 5 mm diameter quartz tube inside a Dewar filled with liquid nitrogen.

The phosphorescence lifetimes were measured using a FluoroMax-4 spectrofluorometer, which is also equipped with a Xe-pulsed lamp operating at up to 25 Hz. The phosphorescence decays are obtained according to a time-gated method. The emission is recorded using a control module that includes a gate-and-delay generator that allows the integration of the signal during a specific period after a flash (delay) and for a predetermined time window. The total signal is accumulated for a large number of exciting pulses.

For the steady-state anisotropy measurements, two Glan-Thompson polarizers are placed in the excitation and emission beams. The

anisotropy r is determined as follows

$$r = \frac{I_{VV} - gI_{VH}}{I_{VV} + 2gI_{VH}} \quad \text{with } g = \frac{I_{HV}}{I_{HH}}$$

where I is the fluorescence intensity. The subscripts denote the orientation (horizontal H or vertical V) of the excitation and emission polarizers, respectively. g is an instrumental correction factor. The proper calibration of the setup was checked using a recent standard method with rhodamine 101 in glycerol.⁴²

The fluorescence lifetimes were measured using a Nano LED emitting at 372 nm as an excitation source with a nano-led controller module, Fluorohub from IBH, operating at 1 MHz. The detection was based on a R928P type photomultiplier from Hamamatsu with a high-sensitivity photon-counting mode. The decays were fitted with the iterative reconvolution method on the basis of the Marquardt/Levenberg algorithm.⁴³ Such a reconvolution technique allows an overall time resolution down to 0.2 ns. The quality of the exponential fits was checked using the reduced χ^2 (≤ 1.2).

The cyclic voltammetry experiments⁴⁴ (using a computer-controlled Princeton 263A potentiostat with a three-electrode single-compartment cell; a saturated calomel electrode in methanol used as a reference was placed in a separate compartment) were performed at 300 K, in Ar-degassed acetonitrile with a constant concentration (0.1 M) of *n*-Bu₄NBF₄. Ferrocene was used as an internal reference.

Semi-empirical quantum chemical calculations were performed using AM1 method (from HYPERCHEM package⁴⁵).

The two-photon absorption measurements were performed with femtosecond mode-locked laser pulse using a Ti:sapphire laser (Spectra-Physics, Mai Tai, pulse duration: ~ 100 fs; repetition rate: 80 MHz; wavelength range: 690–1020 nm). A relative two-photon-induced fluorescence (TPIF) method^{15,46} was employed to measure the two-photon absorption cross sections, δ . A 10^{-4} M solution of fluorescein⁴⁶ in water at pH 11 was used as the reference (r). The value of δ for a sample (s) is given by

$$\delta_s = \frac{S_s \Phi_r \eta_r c_r}{S_r \Phi_s \eta_s c_s} \times \delta_r$$

where S is the detected two-photon induced fluorescence integral area, c the concentration of the chromophores, and Φ is the fluorescence quantum yield of the chromophores. η is the collection efficiency of the experimental setup and accounts for the wavelength dependence of the detectors and optics as well as the difference in refractive indices between the solvents in which the reference and sample compounds are dissolved. The measurements were conducted in a regime where the fluorescence signal showed a quadratic dependence on the intensity of the excitation beam, as expected for two-photon induced emission. For the calibration of the two-photon absorption spectra, the two-photon induced fluorescence signal of each compound was recorded at the same excitation wavelength (λ_{exc} : 782 nm) as that used for fluorescein. The concentration of the solutions was in the range of $3\text{--}4 \times 10^{-4}$ M for compounds. The laser intensity was in the range of $(0.2\text{--}2) \times 10^9$ W/cm². The experimental error on the reported cross section is 15–20%.

The photopolymerization was monitored in situ by real-time Fourier transformed infrared spectroscopy with an AVATAR 360 FTIR spectrometer from Nicolet. A drop of the photocurable formulations is spread out with a calibrated bar on a polypropylene film that is deposited on a BaF₂ pellet. This laminated formulation is then covered by a second polypropylene film in order to minimize the inhibiting effect of oxygen. The formulations were irradiated at 377 nm with a laser diode from (Cube type from Coherent). The conversion rates are obtained from the progressive disappearance of the vinyl C=C stretching vibration band at 1630 cm⁻¹.

The point-by-point exposure experiment was performed using the same femtosecond pulse laser used for TPIF. The formulation was

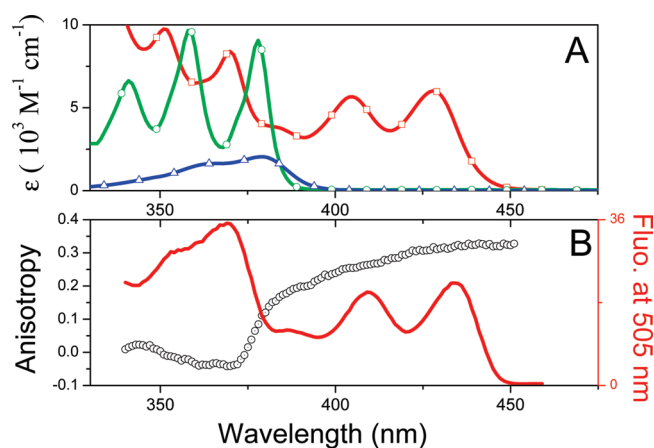


Figure 1. (A) Absorption spectra of ANT-X (squares), ANTH (circles), and TX (triangles) in acetonitrile. (B) Fluorescence excitation spectrum and excitation anisotropy of ANT-X (circles) in glassy matrix of 2-MTHF at 77 K ($\lambda_{\text{em}} = 505$ nm).

poured onto a glass slide and covered with a coverslip. The laser was focused through a lens ($f = 5$ cm). The sample was placed on an X-step motorized stage controlled by a computer. The two-photon polymerized microdots were then recorded and dimensioned using an optical microscope.

The 3D lithographic microfabrication and the point-by-point exposure experiment at 532 nm were performed using a Zeiss Axiovert inverted a 3D microfabrication module (www.teemphotonics.com) with a frequency doubled Nd:YAG microlaser ($\lambda_{\text{exc}} = 532$ nm, pulse duration 0.5 ns, maximum pulse energy 4 μJ , repetition 6.5 kHz). Ebecryl 605 monomer was preferred to SR344 because a better stability of the μ -structures was observed during the microfabrication step. This effect should be ascribed to the high viscosity of Ebecryl 605. The two-photon excitable resin was poured on a coverslip and then mounted on a computer-controlled 3D piezoelectric stage allowing the translation relative to the laser focal point. The incident beam was focused through an oil objective (100 X, 1.25 NA), which leads to 300 nm radial spot size (1/e Gaussian). The average laser power and scan speeds were 20 μW and 60 $\mu\text{m/s}$, respectively. The unexposed resin was washed away after fabrication.

3. RESULTS AND DISCUSSION

Photophysical and Electronic Properties of ANT-X. Panel (A) of Figure 1 shows the absorption spectra of ANT-X and its model chromophores, TX and ANTH, in acetonitrile. The steady-state excitation anisotropy of ANT-X collected in glassy matrix of 2-methyl tetrahydrofuran (2-MTHF) is also presented in panel (B) of Figure 1. The red energy part of the absorption spectrum clearly exhibits a vibronic structured band with a maximum located at 428 nm. This band is specific to ANT-X because it is neither observed for TX nor for ANTH, such a band exhibits a low intensity with ϵ_{MAX} of about $6000 \text{ M}^{-1} \text{ cm}^{-1}$. As previously observed for thioxanthone derivatives,^{27–30} the weakly allowed character of the last absorption band should be ascribed to a strong electronic coupling between two electronic transitions with distinctive symmetries: a forbidden $n\pi^*$ transition mainly localized on the carbonyl group and a low lying $\pi\pi^*$ transition involving an electronic delocalization along the aromatic ring. It is noteworthy that both transitions are very close in energy because a constant anisotropy with a mean value of 0.32 ± 0.01 is measured in this spectral region (Figure 1B). In the

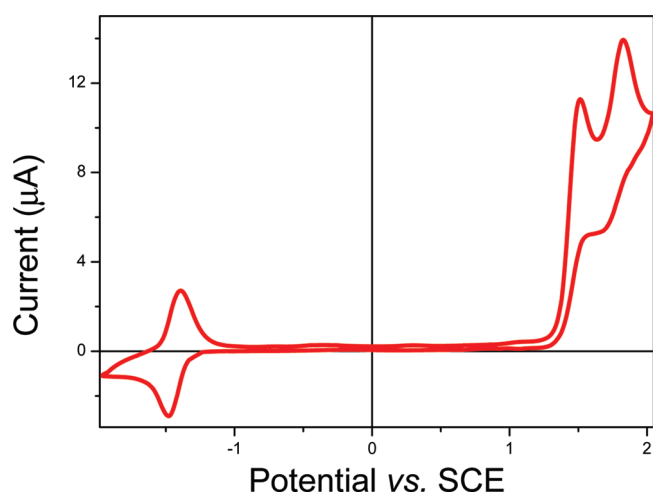


Figure 2. Cyclic voltammogram of ANT-X in acetonitrile + (nBu)₄NPF₆ (0.1 M) on platinum electrode at 100 mV s⁻¹ (concentration of ANT-X: 2.3 × 10⁻³ M).

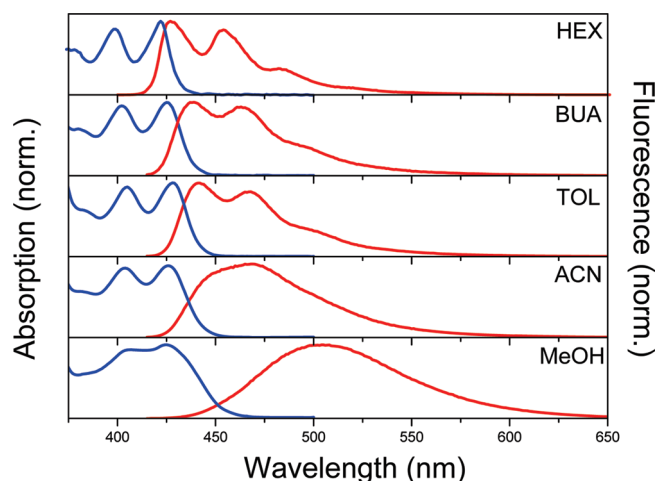


Figure 3. Normalized absorption and fluorescence spectra of ANT-X in solvents of different polarity.

340–410 nm range, a comparison with the absorption spectra of the model chromophores indicates that the absorption spectrum of ANT-X is mainly composed of electronic transitions equivalent to those present in the absorption spectra of TX and ANTH. For instance, the characteristic band of ANTH, which is assigned to its S₀–S₁ transition,⁴⁷ is clearly observed in the high energy side of the absorption spectrum of ANT-X and despite a slight band hypsochromy this structured band conserved its intensity. Similar observations can be done for transitions relative to the thioxanthone fragment, whose associated bands are hardly detected throughout a shoulder located at 380 nm. Moreover, the excitation anisotropy spectrum, which decreases sequentially when going from 420 to 370 nm, corroborates the presence of these transitions (Figure 1B). A first stabilization of the anisotropy is noticed in the 385–395 nm range with a value close to 0.2, which is consistent with the presence of transitions centered on thioxanthone moiety. A second plateau is reached between 360 and 370 nm with an anisotropy of about -0.03 ± 0.02 , which should correspond to transitions relative to anthracene bar. In the same manner, the electrochemical properties of

Table 1. Spectroscopic Data of ANT-X in Various Solvents

<i>n</i> ^o	solvent	λ_a^{\max} (nm) ^a	λ_f^{\max} (nm) ^a	Φ_f	τ (ns)	k_f (10 ⁷ s ⁻¹)	k_{nr} (10 ⁷ s ⁻¹)
1	HEX	398, <u>422</u>	<u>427</u> , 457	0.014	0.25	5.6	395
2	TOL	405, <u>429</u>	<u>441</u> , 467	0.018	0.29	6.2	340
3	EOE	400, <u>423.5</u>	<u>433.5</u> , 460	0.015	0.26	5.8	380
4	BTA	403, <u>425</u>	<u>439</u> , 463	0.015	0.29	5.2	340
5	ETA	402, <u>425</u>	<u>441</u> , 465	0.015	0.31	4.8	320
6	MTHF	402, <u>425</u>	<u>438</u> , 462	0.021	—	—	—
7	THF	403, <u>426.5</u>	<u>441</u> , 465	0.016	0.32	5.0	310
8	CH ₂ Cl ₂	406, <u>429.5</u>	<u>452.5</u> , <u>471</u>	0.016	0.32	5.0	310
9	DMF	406, <u>429</u>	454, 470	0.018	0.40	4.5	245
10	ACN	404, <u>426</u>	<u>449</u> , <u>469</u>	0.018	0.37	4.9	265
11	EtOH	403, <u>425</u>	494	0.023	0.59	3.9	165
12	MeOH	405, <u>425</u>	505	0.023	0.70	3.3	140

^a In case of double maxima, the main one is underlined.

ANT-X can be compared to those of the model chromophores. Figure 2 depicts the cyclic voltammogram of ANT-X recorded in acetonitrile. The cathodic part corresponds to the reversible reduction of ANT-X. The corresponding half-wave potential has a value of about -1.46 V/SCE, which is closer to the reduction potential of TX (-1.66 V/SCE) than to that of ANTH (-1.96 V/SCE). This indicates that the radical anion of ANT-X probably has its negative charge localized on the thioxanthone fragment with possibly an extended conjugation along a phenyl moiety, which should favor a better stabilization of the radical anion. At high potential, ANT-X shows two irreversible oxidation waves; their respective maximum oxidation waves have a potential at 1.47 V/SCE and 1.80 V/SCE. These values correspond to the oxidation potential of anthracene (1.37 V/SCE) and thioxanthone (1.75 V/SCE) moieties, respectively.

Figure 3 shows the normalized absorption and fluorescence spectra of ANT-X in various solvents of increasing polarity. The corresponding spectroscopic data are listed in Table 1. The absorption spectrum of ANT-X is slightly influenced by solvent polarity. In apolar and medium polar solvents, the absorption and emission bands clearly exhibit a mirror image relationship that indicates a weak electronic and/or geometrical change between the ground and excited state. However, in a highly polar solvent, such a mirror image effect disappears due to a more pronounced red-shift of the fluorescence band that concomitantly loses its vibronic structuration. Moreover, this band red-shift is even pronounced for the protic solvent as methanol. For instance, the last absorption band of ANT-X is located at 426 nm in methanol, which is similar to that observed for acetonitrile; however, the corresponding fluorescence band is strongly shifted to the red region with a maximum at 505 nm as compared to the emission band in acetonitrile centered at 469 nm. Sensitivity to hydrogen bonding at an excited state is therefore suggested for ANT-X. Similarly to TX, this abnormal fluorescence red-shift should be ascribed to the formation of a S₁-complex between the excited chromophore and the solvent molecules as recently proposed by Kryskowiak et al.⁴⁸ for TX. In pure dielectric solvents, the Stokes shift of ANT-X is roughly multiplied by a factor of 10 going from hexane to acetonitrile. The change in the dipole moment between the ground and excited states, $\Delta\mu_{ge}$, can be evaluated from the solvation effects on the Stokes shift⁴⁹

according to the following relation

$$hc(v_{abs} - v_{flu}) = \frac{1}{4\pi\epsilon_0} \frac{2\Delta\mu_{ge}^2}{a^3} \times \left[\frac{\epsilon - 1}{2\epsilon + 1} - \frac{n^2 - 1}{2n^2 + 1} \right] + const \quad (1)$$

In this expression, ϵ is the relative permittivity and n the refractive index of the solvent, h is the Planck constant and c is the speed of light. The Onsager radius a defined as the solvent shell around

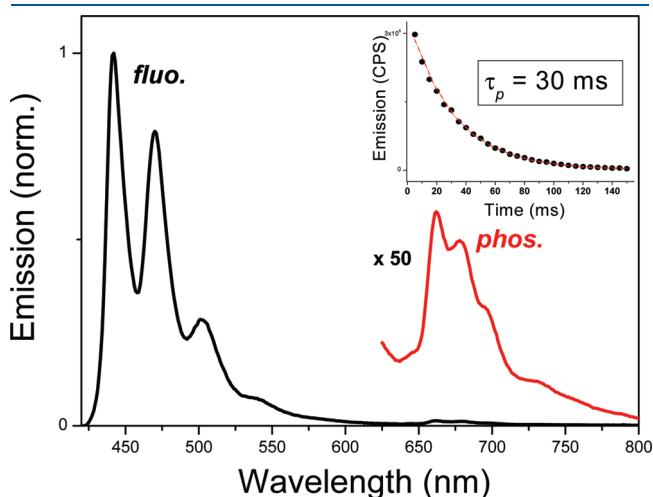


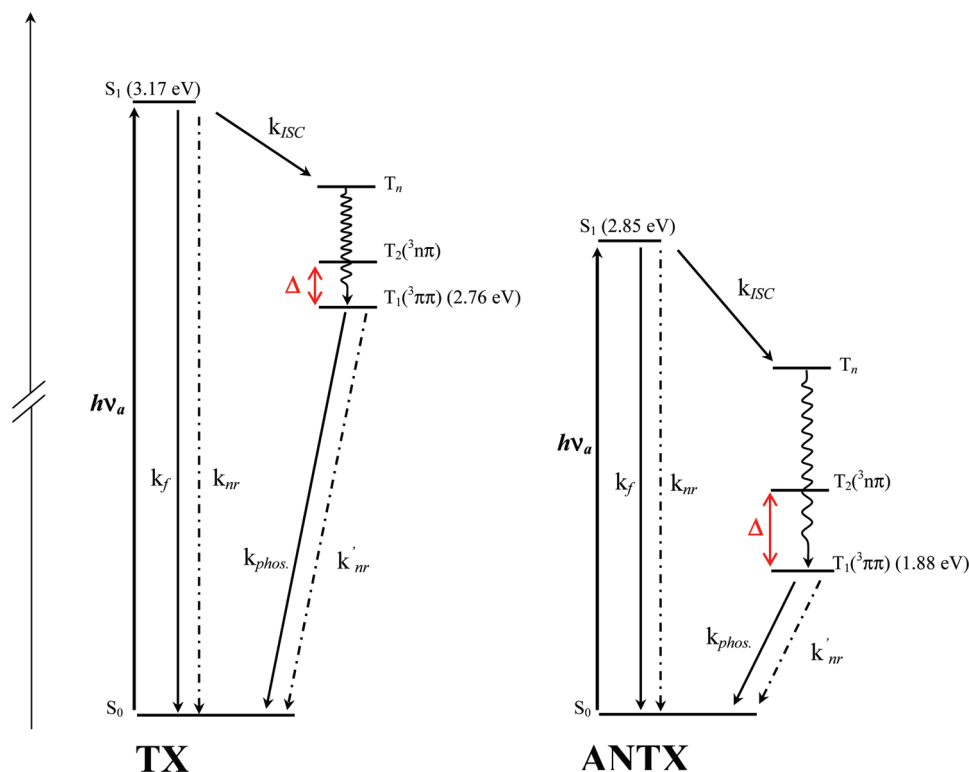
Figure 4. Normalized emission spectra of ANT-X in glassy matrix of 2MTHF (77 K). Inset: Decay profile of the phosphorescence signal monitored at 660 nm.

the molecule was estimated to a value of 5.5 Å from the full-geometry optimization of ANT-X by AM1 method.⁴⁵ The change in dipole moment from ground to excited state is then estimated at 7.7 ± 0.8 D, which is three times larger than $\Delta\mu_{ge}$ measured for TX.^{28,29,50}

From Table 1, one can observe that the nonradiative deactivation process constitutes the major deactivation pathway of the excited singlet state. For instance, the nonradiative rate constant (k_{nr}) is at least 50 times larger than the radiative one (k_r) in nonprotic solvents. By analogy with TX, one of the main deactivation process at the S_1 state should be assigned to an efficient S_1-T_n intersystem crossing (ISC) due to the presence of the ketone function which is well known to promote electronic spin-orbit coupling.^{51–53}

Figure 4 shows the emission spectrum of ANT-X in glassy matrix of 2-MTHF at 77 K. The fluorescence band located in the 425–625 nm range has a maximum emission at 442 nm, whereas the red energy part of the spectrum displays a low emissive band, which corresponds to the phosphorescence emission of ANT-X. Its emission lifetime has a value of about 30 ms, which is clearly longer than that of TX (i.e., 9 μ s) but matches better the phosphorescence lifetime of ANTH (i.e., 40 ms). The phosphorescence maximum located at 660 nm leads to a low triplet energy (T_1) of about 1.88 eV, which is very close to the T_1 energy of ANTH.⁴⁷ Moreover, the large energy gap measured between S_1 and T_1 (~ 0.93 eV from Figure 4) corroborates the presence of high lying T_n levels that should be implicated in the ISC process as depicted in Scheme 2. The similarity observed between the phosphorescence of ANT-X and ANTH indicates that the T_1 state of ANT-X dominantly exhibits a $\pi\pi^*$ character with an electronic symmetry comparable to that of the T_1 state of ANTH. However, as will be discussed hereafter, the electronic

Scheme 2. Simplified Scheme for the Photophysics of TX and ANT-X



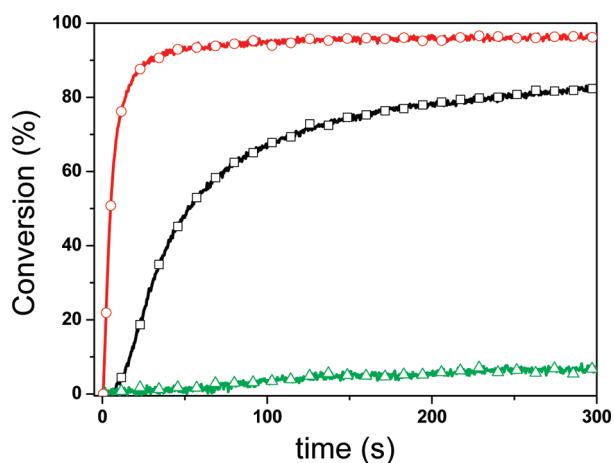


Figure 5. Conversion vs time curves for photopolymerization of diacrylate monomer (SR344). λ_{exc} : 377 nm. Irradiance: 4.5 mW cm^{-2} . Photoinitiating systems: ANTH/ MDEA, 0.15 wt %/4 wt % (triangles). ANT-X/ MDEA, 0.08 wt %/4 wt % (squares). TX/ MDEA, 0.15 wt %/4 wt % (circles).

configuration of the T_1 state of ANT-X should not be considered as a pure $^3\pi\pi^*$ state but should imply a thermal activated vibronic mixing with a high-lying $^3n\pi^*$ state.^{51–53} This so-called “proximity effect”, which has been extensively rationalized for TX,^{27–30,36} will have strong consequence on the reactivity of the T_1 state of ANT-X.

Free Radical Photoinitiating Ability of ANT-X. Even though a clear similarity appears between both phosphorescence emissions of ANT-X and ANTH, the reactivity of their respective T_1 states as hydrogen abstractors is clearly different. This difference can be highlighted by a comparison of the free radical photoinitiating ability of each chromophore as presented in Figure 5. The conversion rates of acrylate double bonds from formulations containing the chromophores dissolved in diacrylate monomer are monitored upon irradiation at 377 nm. These formulations all contain 4 wt % of N-methyl diethanolamine (MDEA), which is used as hydrogen donor reactant. In this case, the free radical photopolymerization first proceeds through the generation of highly reactive α -amino alkyl radicals ($\text{H}_2\text{C}^\bullet\text{—NR}_2$), which are generated by a H-transfer reaction from MDEA to the excited triplet state of the chromophore. A photoinitiation step then occurs by addition of the α -amino alkyl radicals on the acrylate double bonds.⁵⁴ From Figure 5, we can clearly notice that ANTH is a very weak efficient photoinitiator with respect to ANT-X and TX. For instance, the double bonds conversion hardly reaches 5% after 100 s irradiation, whereas ANT-X and TX lead to a conversion of 70% and 95%, respectively. The higher hydrogen abstract ability of the T_1 state of ANT-X confirms the involvement of a close lying $^3n\pi^*$ state, which is considered to be highly reactive toward H-transfer.³⁶ In the same manner, if we compare the photoinitiating properties of ANT-X and TX, it is clear that TX promotes a much faster conversion rate. At half-maximum conversion, the rate for the formulation with TX is 10 times higher as compared with that with ANT-X. When going from TX to ANT-X, the electronic conjugation should promote a better energy stabilization of the $^3\pi\pi^*$ state with respect to the $^3n\pi^*$ one. As depicted in Scheme 2, the increase in energy gap between these two levels (Δ) should lead to less mixing with the highly

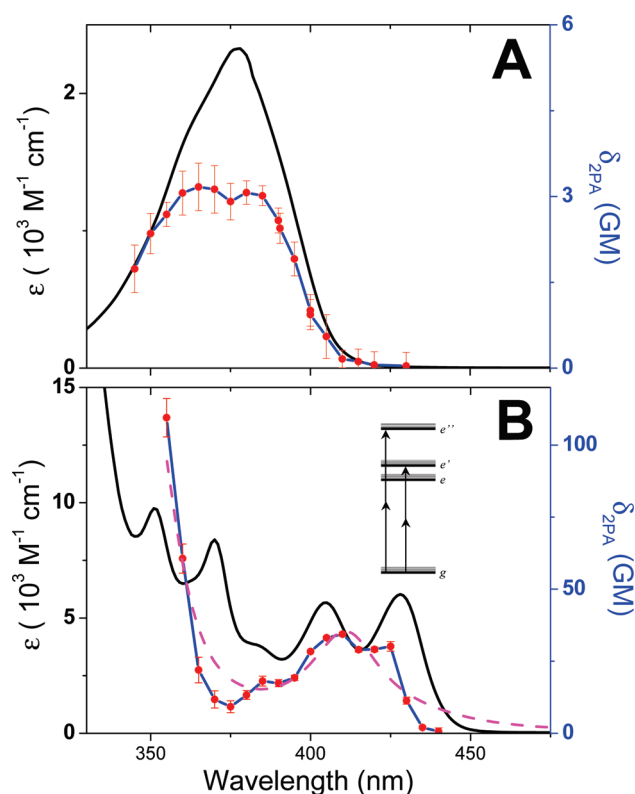


Figure 6. Linear absorption and 2PA (circles) spectra of TX in methanol (A) and of ANT-X in acetonitrile (B). (B) Theoretical fitting (dashed line) derived from the SOS model based on a four-level energy scheme depicted in the inset.

reactive $^3n\pi^*$ state. However, the reduction of the “proximity effect” is sufficiently moderate to conserve a satisfactory reactivity at the T_1 state. Moreover, the relative decrease in the reactivity of the T_1 state for ANT-X constitutes a necessary compromise so as to improve the two-photon absorption properties of this free radical photoinitiator.

Two-Photon Initiating Properties of ANT-X. The two-photon absorption (2PA) cross sections were obtained by two-photon induced fluorescence (TPIF) method^{15,46} using femtosecond pulse laser as excitation source. Figure 6 shows the one- and two-photon absorption (2PA) spectra of the chromophores. The 2PA spectra are plotted against half the excitation wavelength to allow a direct comparison with the linear absorption spectra. Both lowest-energy 2PA bands nicely coincide with their respective linear lowest-energy absorption bands, which suggests that the $S_0 \rightarrow S_1$ transitions are two-photon active. However TX exhibits a very low two-photon absorption cross section (δ) with a maximum value of about $3 \pm 1 \text{ GM}$ at 710 nm. This very low value is in good accordance with that previously measured by the Z-scan method.²⁶ The lowest-energy 2PA band of ANT-X is moderately intensive with a δ_{MAX} of about $35 \pm 3 \text{ GM}$ at 810 nm. In the first approximation, the substantial increase in δ as compared with TX should be ascribed to the combined effects of: (i) a larger $\Delta\mu_{\text{ge}}$, which is multiplied by a factor 3 and (ii) an increase in the transition moment M_{ge} between the ground and the first excited states. This latter parameter can be calculated by integration of the linear last absorption band, $\varepsilon(\nu_a)$, according

to the following relation⁵⁵

$$M_{ge} = \left[\frac{3hc10^3 \ln 10}{8\pi^3 N_L n} \int \varepsilon(\nu_a) d(\ln \nu_a) \right]^{1/2} \quad (2)$$

where N_L corresponds to the Avogadro's number. Because **ANTX** does not have a clear lowest-lying single band, the spectral region where integration was taken over was chosen for $\lambda_{abs} > 420$ nm, which corresponds to the first plateau observed in the excitation anisotropy spectrum of **ANTX** (Figure 1). The transition dipole moment of **ANTX** is then estimated to a value of about 2.9 D, which is two times larger than that obtained for **TX** (i.e., M_{ge} : 1.4 D). It is to be noted that both transition dipole moments are relatively low due to the $n\pi^*$ character of the $S_0 \rightarrow S_1$ transitions. Even though the low energy 2PA band of **ANTX** is clearly more intensive than that of **TX**, more interesting is the high energy side of the 2PA spectrum of **ANTX**, whose intensity undergoes a very strong increase and reaches a value of about 110 ± 10 GM at 710 nm. In this case, **ANTX** shows a two-photon cross section that is 30 times larger than that of **TX**. Such a monotonic increase in the high frequency region can be analyzed in the frame of the sum-overstates (SOS) formalism.^{56,57} Similarly to the model used by Corrêa et al in order to fit the 2PA spectra of perylene tetracarboxylic derivatives,^{58,59} we also adopt a four-level energy model involving the ground (g) and the lowest excited (e) states and two low-lying excited states e' and e'' . This model assumes two competitive 2PA transitions with distinctive final states (e' and e'') but mediated by the same one-photon absorption allowed state (e) (inset of Figure 6). Even though **ANTX** exhibits a moderate change of the permanent dipole moment upon excitation ($\Delta\mu_{ge} \sim 8$ D), the dipolar term⁶⁰ should account for a substantial fraction of the 2PA activity. Moreover, the reduced symmetry in this system suggests that dipole selection rules are equivalent for 1PA and 2PA. Therefore, the term describing 2PA into the dipole-allowed 1PA state has been added in the approximation. The dependence of the 2PA cross section on the excitation laser frequency, ν , can be expressed according to the following equation

$$\delta(\nu) \propto \frac{\nu^2}{(\nu_{ge} - \nu)^2 + \Gamma_{ge}^2} \times \left[\frac{M_{ge}^2 M_{ee'}^2 \Gamma_{ge'}}{(\nu_{ge'} - 2\nu)^2 + \Gamma_{ge'}^2} + \frac{M_{ge}^2 M_{ee''}^2 \Gamma_{ge''}}{(\nu_{ge''} - 2\nu)^2 + \Gamma_{ge''}^2} + \frac{M_{ge}^2 \Delta\mu_{ge}^2 \Gamma_{ge}}{(\nu_{ge} - 2\nu)^2 + \Gamma_{ge}^2} \right] \quad (3)$$

where $\nu_{\alpha\beta}$, $M_{\alpha\beta}$, and $\Gamma_{\alpha\beta}$ are respectively the transition energy, the transition dipole moment, and the corresponding damping factor for the transition $\alpha \rightarrow \beta$. This latter parameter was fixed to 0.1 eV for $\Gamma_{ge'}$ and $\Gamma_{ge''}$, such a value is a typical damping width for aromatic molecules.^{15,61} ν_{ge} has a value of about 2.85 eV and Γ_{ge} is estimated to 0.15 eV, which corresponds to the half width at half-maximum of the lowest-energy band of the linear absorption spectrum. Finally, the value of the high transition frequency ($\nu_{ge''}$) was fixed to 3.82 eV, which corresponds to the energy associated to the maximum absorption peak at the high energy side of the one-photon spectrum. All other parameters (A_i) are kept floating in the fitting procedure (i.e., $A_1 = M_{ge}^2 M_{ee'}^2 \Gamma_{ge'}$, $A_2 = M_{ge}^2 M_{ee''}^2 \Gamma_{ge''}$, $A_3 = \nu_{ge'}$). Panel (B) of Figure 6 shows the fitting

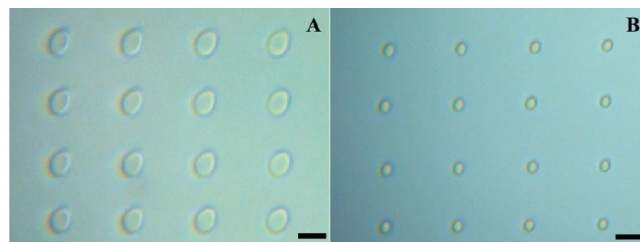


Figure 7. Two-photon polymerization voxels fabricated with femto-second laser direct writing by 2PA photopolymerization (λ_{exc} : 710 nm; average power: 70 mW; exposure time: 30 s). Diacrylate formulations of Ebecryl 605 with (A) **ANTX**/MDEA, 0.08 wt %/4 wt % and (B) **TX**/MDEA, 0.05 wt %/4 wt %. Scale bar: 20 μ m.

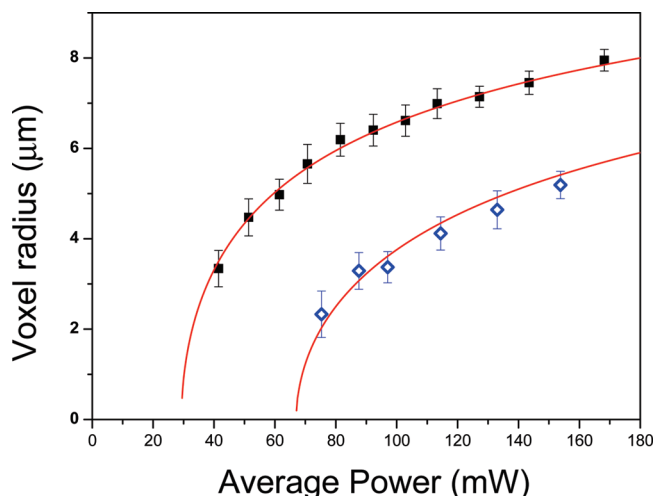


Figure 8. Variation of the polymerized voxel radius as a function of the incident average power (squares: **ANTX**; diamonds: **TX**; λ_{exc} : 710 nm; time exposure: 20 s). The solid line corresponds to the best fit data using eq 4. The least-squares fits were performed by linking the instrumental parameter (F) for both curves.

curve derived from eq 3. Even though the vibronic structure of the lowest-energy band cannot be reproduced at this theoretical level, the evolution of 2PA spectrum is well reproduced with a resonant band at 823 nm and a strong increase of δ below 750 nm. Moreover, the results from the curve fitting indicate that the low-lying 2PA transition ($g \rightarrow e'$) is located at 3.02 eV (411 nm), which is reasonably close to the energy of the transition located at the blue side of the longest wavelength one-photon absorption band.

Therefore, a relevant strategy to optimize the two-photon initiating ability of **ANTX** should consist in exciting the chromophore at 710 nm. Additionally, a direct comparison with **TX** used as reference system becomes straightforward. Figure 7 shows the micrograph of polymerized microdots obtained upon focusing the femtosecond pulse laser beam into laminated diacrylate formulations containing MDEA (4 wt %) and the chromophores at the same concentration (2.5×10^{-3} M). The presence of MDEA as a hydrogen donor is necessary otherwise the two-photon polymerization is hardly observed. With the same irradiation conditions, the microdots obtained from the formulation with **TX** have an average diameter of 6 ± 0.5 μ m, whereas those generated with formulation containing **ANTX**

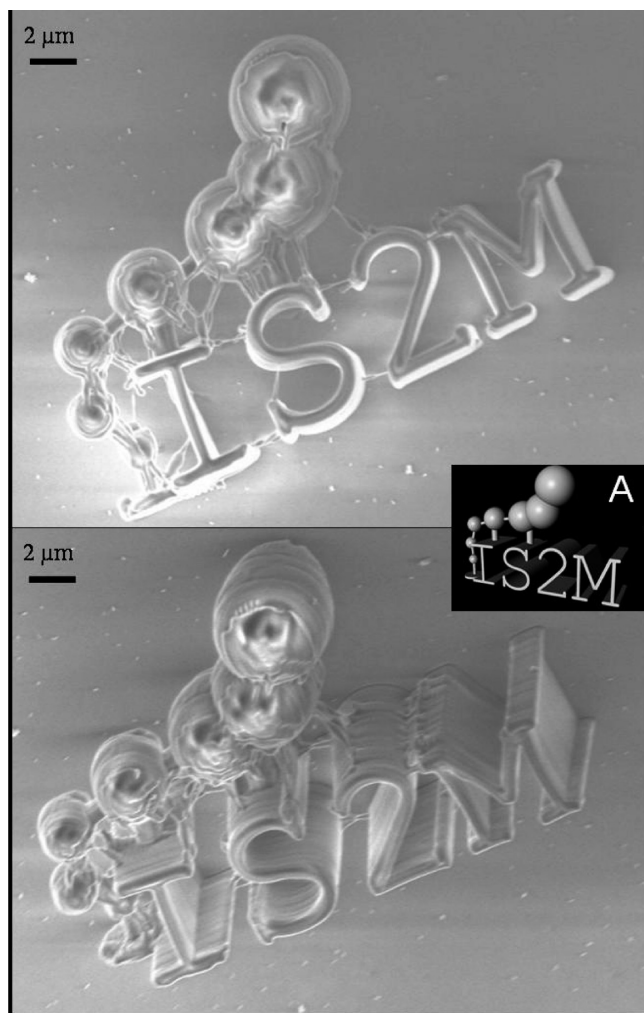


Figure 9. SEMs of a microstructure fabricated by TPIP upon excitation at 532 nm. Inset: model master.

have a much larger diameter of $18 \pm 1 \mu\text{m}$. We have therefore a clear indication that **ANTX** exhibits a lower two-photon polymerization threshold (E_{th}) as compared with **TX**. E_{th} , which is defined as the local absorbed energy density below which the polymer is not obtained,⁶² can be evaluated from point-by-point exposure experiments.^{7,17,54,62,63} Figure 8 displays the growth of the microdots radius in function of the incident power (P) for a fixed exposure time Δt . It can be observed that equivalent incident energy always leads to larger microdots for **ANTX**. This result is completely different from that observed for linear polymerization (Figure 5). Using the formalism recently proposed by Lee et al.,⁷ which provides a direct access to E_{th} , the radius of the polymerized microdots (r) can be expressed as

$$r = F \sqrt{\ln \frac{(2P)^2 \Delta t}{\pi^2 F^4 E_{\text{th}}}} \quad (4)$$

In this expression, it is assumed that the incident laser intensity presents a Gaussian profile in the focal plan. F is a constant parameter that encompasses the instrumental conditions as the excitation wavelength, the numerical aperture of the focused laser, and the refractive index of the medium. Using **TX** as the reference, the least-squares fits of both experimental data with

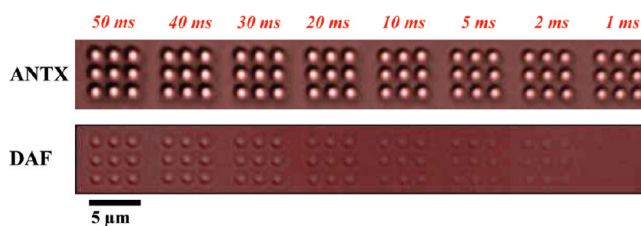


Figure 10. Arrays of microdots written (λ_{exc} : 532 nm; power: 1.5 mW; NA: 0.64) in diacrylate formulations of Ebecryl 605 with (**ANTX**/MDEA, 0.08 wt %/4 wt %) and (**DAF**, 0.20 wt %).

eq 4 indicates that E_{th} is divided by a factor of 5 going from **TX** to **ANTX**. Such a substantial decrease of E_{th} corroborates the combined effect of a high reactivity of the excited triplet state of **ANTX** and remarkable two-photon absorption ability at 710 nm.

From eq 3, it suggested that the two-photon cross section can be strongly enhanced when the laser excitation frequency approaches the one-photon transition frequency (ν_{ge}). In this case, the detuning factor ($\nu_{\text{ge}} - \nu$) in the denominator of the first term decreases. This “so-called” one-photon resonance enhancement in the 2PA spectrum has been extensively investigated by Drobizhev et al.^{64–66} for porphyrin derivatives that undergo a large increase in δ when excited near their linear absorption Q bands. To illustrate such a similar effect for **ANTX** and qualitatively demonstrate the potential for 2PA stereolithography, we produced a 3D microstructure by exciting the resin with **ANTX** at 532 nm using a nanosecond pulse microlaser. Figure 9 shows the scanning electron micrograph of the 3D microstructure fabricated at an average power of 20 μW . The pattern is impressed into the resin by the relative translation of the laser focus within the material then the final structure is obtained by dissolving away the unexposed formulation. The formation of a three-dimensional microstructure with a variety of dimensions was thus achieved with good fidelity replication of the master model displayed in the inset of Figure 9. This practical demonstration first illustrates that **ANTX** remains two-photon activable near the one-photon allowed absorption region and confirms that this new system constitutes an efficient two-photon initiator.

Finally, to demonstrate the relevance of using **ANTX** as a highly sensitive two-photon initiator upon excitation nearby the one-photon absorption band, we compare its photoinitiating efficiency with that of a diaminofluorene derivative used as one-component photoinitiator (**DAF**, Scheme 1). The two-photon absorption properties of this latter chromophore have been extensively studied by Belfield et al.,^{1,8,10,16} and its two-photon initiating ability has been clearly established.^{11,32,54} As previously reported by Rumi et al.² for the 4,4'-dialkylamino *trans*-stilbene, the photoinitiating mechanism mainly implies an electron transfer from the excited triplet chromophore to the acrylate monomer, which produces the radical species. In Figure 10, we show an example of a transmitted micrograph where a microdots array was written within acrylate resins containing **DAF** and **ANTX** at the same concentration. The laser excitation power was maintained at 1.5 mW in both cases, but the time exposure was gradually decreased from 50 to 1 ms. An objective with a numerical aperture of 0.64 was employed in this case. For each time exposure, nine dots delimiting a $4 \mu\text{m} \times 4 \mu\text{m}$ square were fabricated. It is clear that the microdots generated with the formulation containing **ANTX** are hardly affected by the time exposure decrease, which indicates that the photopolymerization

threshold is reached in all cases. This effect strikingly contrasts with the strong changes observed for the microdots obtained with DAF. First, it should be noted that the microdots are less bright than those obtained with ANTX for the same time exposure. The contrast between the polymerized material and the original resin is due to a significant increase of the refractive index upon polymerization. Therefore, one can reasonably assume that the conversion of the acrylate double bond is locally enhanced for the resin with ANTX with respect to that with DAF. In addition, it should be pointed out that the microdots obtained with DAF disappear with a decrease in the time exposure. For instance, no microstructure is detected upon 1 ms excitation. In this case, the incident energy density is insufficient to promote the photoinitiation. Such a local effect has been assigned to the very high oxygen sensitivity of the triplet excited DAF,⁶⁷ which induces an efficient quenching process to the detriment of the initiation step. Even though the triplet states of thioxanthone derivatives are also quenched by oxygen,^{36,37,68} it appears that this inhibition pathway does not impact the photoinitiation yield with the same magnitude as it can be observed for DAF. Hence, we clearly evidence here that ANTX exhibits a much higher reactivity as the reference system.

CONCLUSION

The photophysical and electronic properties of a new hybrid anthracene–thioxanthone system with a noncollinear configuration architecture were thoroughly described. Such a design strategy was adopted so as to extend the electronic conjugation along the aromatic rings and to maintain active the strong vibronic coupling between the two lowest excited states at singlet and triplet manifolds. As a consequence, ANTX both gathers the characteristic features of a very efficient hydrogen abstractor and a two-photon activable chromophore with a remarkable 2PA cross section that is 30 times larger than that measured for TX at 710 nm. A substantial improvement of the two-photon polymerization efficiency was thereby demonstrated with the lowering of the polymerization threshold, which was divided by a factor of 5 with respect to TX. We also showed that the two-photon absorption spectrum of ANTX, which undergoes a strong increase below 750 nm, can be fitted by means of a sum–overstates formalism. A four-state model was then necessary to account for the observed spectral shape. At this theoretical level, a resonant enhancement of the nonlinearity was also suggested in the spectral region near the linear absorption. Such an effect has been qualitatively corroborated by the two-photon activation of ANTX at 532 nm, leading to the fabrication of a complex 3D microstructure. From this excitation mode, we finally demonstrated the superior efficiency of ANTX with respect to a 2,7-diaminofluorene derivative, which is commonly used as two-photon initiator.

AUTHOR INFORMATION

Corresponding Author

*E-mail: jean-pierre.malval@uha.fr (J.-P.M.); mingjin@tongji.edu.cn (J.M.).

ACKNOWLEDGMENT

Support from the Agence Nationale de la Recherche “Projet Blanc : 2PAGmicrofab” (ANR 2010-BLAN-0815-01) is gratefully acknowledged.

REFERENCES

- (1) Belfield, K. D.; Schafer, K. J.; Liu, Y.; Liu, J.; Ren, X.; Stryland, E. W. V. *J. Phys. Org. Chem.* **2000**, *13*, 837–849.
- (2) Cumpston, B. H.; Ananthavel, S. P.; Barlow, S.; Dyer, D. L.; Ehrlich, J. E.; Erskine, L. L.; Heika, A. A.; Kuebler, S. M.; Lee, I.-Y. S.; McCord-Maughon, D.; Qin, J.; Röckel, H.; Rumi, M.; Wu, X.-L.; Marder, S. R.; Perry, J. W. *Nature* **1999**, *398*, 51–54.
- (3) Kawata, S.; Sun, H.-B.; Tanaka, T.; Takada, K. *Nature* **2001**, *412*, 697.
- (4) Lee, K. S.; Kim, R. H.; Yang, D. Y.; Park, S. H. *Prog. Polym. Sci.* **2008**, *33*, 631–681.
- (5) Maruo, S.; Nakamura, O.; Kawata, S. *Opt. Lett.* **1997**, *22*, 132–134.
- (6) Sun, H.-B.; Kawata, S. *Two-Photon Photopolymerization and 3D Lithographic Microfabrication*; Springer-Verlag: Berlin, 2004; Vol. 170.
- (7) Lee, K.-S.; Yang, D.-Y.; Park, S. H.; Kim, R. H. *Polym. Adv. Technol.* **2006**, *17*, 72–82.
- (8) Belfield, K. D.; Morales, A. R.; Kang, B.-S.; Hales, J. M.; Hagan, D. J.; Stryland, E. W. V.; Chapela, V. M.; Percino, J. *Chem. Mater.* **2004**, *16*, 4634–4641.
- (9) Hales, J. M.; Hagan, D. J.; Stryland, E. W. V.; Schafer, K. J.; Morales, A. R.; Belfield, K. D.; Pacher, P.; Kwon, O.; Zojer, E.; Bredas, J. L. *J. Chem. Phys.* **2004**, *121*, 3152–3160.
- (10) Belfield, K. D.; Schafer, K. J.; Mourad, W.; Reinhardt, B. A. *J. Org. Chem.* **2000**, *65*, 4475–4481.
- (11) Martineau, C.; Anémian, R.; Andraud, C. W., I.; Bouriau, M.; Baldeck, P. L. *Chem. Phys. Lett.* **2002**, *362*, 291–295.
- (12) He, G. S.; Tan, L.-S.; Zheng, Q.; Prasad, P. N. *Chem. Rev.* **2008**, *108*, 1245–1330.
- (13) Lu, Y.; Hasegawa, F.; Goto, T.; Ohkuma, S.; Fukuhara, S.; Kawazu, Y.; Totani, K.; Yamashita, T.; Watanabe, T. *J. Lumin.* **2004**, *110*, 1–10.
- (14) Zhang, X.; Yu, X. Q.; Sun, Y.; Wu, Y.; Feng, Y.; Tao, X.; Jiang, M. *Mater. Lett.* **2005**, *59*, 3485–3488.
- (15) Rumi, M.; Ehrlich, J. E.; Heikal, A.; Perry, J. W.; Barlow, S.; Hu, Z. Y.; McCord-Maughon, D.; Parker, T. C.; Rockel, H.; Thayumanavan, S.; Marder, S. R.; Beljonne, D.; Brédas, J. L. *J. Am. Chem. Soc.* **2000**, *122*, 9500–9510.
- (16) Belfield, K. D.; Bondar, M. V.; Hernandez, F. E.; Przhonska, O. V.; Yao, S. J. *Phys. Chem. B* **2007**, *111*, 12723–12729.
- (17) Lemerrier, G.; Mulatier, J. C.; Martineau, C.; Anémian, R.; Andraud, C.; Wang, I.; Stephan, O.; Amari, N.; Baldeck, P. L. *C.R. Chimie* **2005**, *8*, 1308–1316.
- (18) Belfield, K. D.; Ren, X.; Stryland, E. W. V.; Hagan, D. J.; Dubikovskiy, V.; Miesak, E. J. *J. Am. Chem. Soc.* **2000**, *122*, 1217–1218.
- (19) Li, X.; Zhao, Y.; Wu, J.; Shi, M.; Wu, F. *J. Photochem. Photobiol., A* **2007**, *190*, 22–28.
- (20) Zhao, Y.; Li, X.; Wu, F.; Fang, X. *J. Photochem. Photobiol., A* **2006**, *177*, 12–16.
- (21) Roffey, C. *Photogeneration of Reactive Species for UV-Curing*; Sussex, U.K.: Wiley, 1997.
- (22) Eaton, D. F. In *Advanced Photochemistry*; Volman, D., Gollnick, K., Hammond, G., Eds.; Wiley: New York, 1986; Vol. 14.
- (23) Lougnot, D. J.; Turck, C.; Fouassier, J. P. *Macromolecules* **2002**, *22*, 108–116.
- (24) Malval, J.-P.; Dietlin, C.; Allonas, X.; Fouassier, J.-P. *J. Photochem. Photobiol., A* **2007**, *192*, 66–73.
- (25) Fouassier, J. P. *Photoinitiation, Photopolymerization, and Photocuring*; Hanser: Munich, 1995.
- (26) Schafer, K. J.; Hales, J. M.; Balu, M.; Belfield, K. D.; Stryland, E. W. V.; Hagan, D. J. *J. Photochem. Photobiol., A* **2004**, *162*, 497–502.
- (27) Scaiano, J. C. *J. Am. Chem. Soc.* **1980**, *102*, 7747–7753.
- (28) Malval, J.-P.; Graff, B.; Jacques, P. *EPA Newslett.* **2009**, *79*, 37–53.
- (29) Burget, D.; Jacques, P. *J. Lumin.* **1992**, *54*, 177–181.
- (30) Angulo, G.; Grilj, J.; Vauthey, E.; Serrano-Andrés, L.; Rubio-Pons, O.; Jacques, P. *ChemPhysChem* **2010**, *11*, 480–488.
- (31) Förster, T. *Z. Naturforsch.* **1949**, *4*, 321.

- (32) Jin, M.; Malval, J. P.; Versace, D. L.; Morlet-Savary, F.; Chaumeil, H.; Defoin, A.; Allonas, X.; Fouassier, J. P. *Chem. Commun.* **2008**, 48, 6540–6542.
- (33) Lemerrier, G.; Martineau, C.; Mulatier, J. C.; Wang, I.; Stephan, O.; Baldeck, P.; Andraud, C. *New J. Chem.* **2006**, 30, 1606–1613.
- (34) Wu, J.; Shi, M.; Zhao, Y.; Wu, F. *Dyes Pigm.* **2008**, 76, 690–695.
- (35) Xing, J. F.; Chen, W. Q.; Dong, X. Z.; Tanaka, T.; Fang, X. Y.; Duan, X. M.; Kawata, S. *J. Photochem. Photobiol., A* **2007**, 189, 398–404.
- (36) Neumann, M. G.; Gehlen, M. H.; Encinas, M. V.; Allen, N. S.; Corrales, T.; Peinado, C.; Catalina, F. *J. Chem. Soc., Faraday Trans.* **1997**, 93, 1517–1521.
- (37) Encinas, M. V.; Rufs, A. M.; Corrales, T.; Catalina, F.; Peinado, C.; Schmith, K.; Neumann, M. G.; Allen, N. S. *Polymer* **2002**, 43, 3909–3913.
- (38) Ferreira, G. C.; Schmitt, C. C.; Neumann, M. G. *J. Braz. Chem. Soc.* **2006**, 17, 905–909.
- (39) Balta, D. K.; Arsu, N.; Yagci, Y.; Jockusch, S.; Turro, N. J. *Macromolecules* **2007**, 40, 4138–4141.
- (40) Jin, M.; Malval, J.-P.; Morlet-Savary, F.; Chaumeil, H.; Defoin, A.; Batat, P.; Jonusauskas, G. *Phys. Chem. Chem. Phys.* **2009**, 11, 2622–2630.
- (41) Meech, R.; Phillips, D. *J. Photochem.* **1983**, 23, 193–217.
- (42) Prazeres, T. J. V.; Fedorov, A.; Barbosa, S. P.; Martinho, J. M. G.; Berberan-Santos, M. r. N. *J. Phys. Chem. A* **2008**, 112, 5034–5039.
- (43) Connor, D. V.; Phillips, D. *Time Correlated Single Photon Counting*, Academic Press: London, 1984.
- (44) Malval, J.-P.; Chaimbault, C.; Fischer, B.; Morand, J.-P.; Lapouyade, R. *Res. Chem. Intermed.* **2001**, 27, 21–34.
- (45) HYPERCHEM, v. 7.03; Hypercube, Inc.: Gainesville, FL, 2002.
- (46) Xu, C.; Webb, W. W. *J. Opt. Soc. Am. B* **1996**, 13, 481–491.
- (47) Montalti, M.; Credi, A.; Prodi, L.; Gandolfi, M. T. *Handbook of Photochemistry*, 3rd ed.; CRC Press: Boca Raton, FL, 2006.
- (48) Kryskowiak, E.; Maciejewski, A.; Kubicki, J. *ChemPhysChem* **2006**, 7, 597–606.
- (49) Lippert, E. *Elektrochem. Angew. Phys. Chem.* **1957**, 61, 962.
- (50) Abdullah, K. A.; Kemp, T. J. *J. Photochem.* **1986**, 32, 49–57.
- (51) Lai, T.; Lim, E. C. *Chem. Phys. Lett.* **1980**, 73, 244–248.
- (52) Lai, T.-i.; Lim, E. C. *Chem. Phys. Lett.* **1981**, 84, 303–307.
- (53) Lim, E. C. *J. Phys. Chem.* **1986**, 90, 6770–6777.
- (54) Malval, J.-P.; Morlet-Savary, F.; Chaumeil, H.; Balan, L.; Versace, D.-L.; Jin, M.; Defoin, A. *J. Phys. Chem. C* **2009**, 113, 20812–20821.
- (55) Strickler, S. J.; Berg, R. A. *J. Chem. Phys.* **1962**, 37, 814.
- (56) Orr, B. J.; Ward, J. F. *Mol. Phys.* **1971**, 20, 513.
- (57) Kamada, K.; Ohta, K.; Iwase, Y.; Kondo, K. *Chem. Phys. Lett.* **2003**, 372, 386–393.
- (58) Corrêa, D. S.; Oliveira, S. L.; Misoguti, L.; Zilio, S. C.; Aroca, R. F.; Constantino, C. J. L.; Mendonça, C. R. *J. Phys. Chem. A* **2006**, 110, 6433–6438.
- (59) Oliveira, S. L.; Corrêa, D. S.; Misoguti, L.; Constantino, C. J. L.; Aroca, R. J.; Zilio, S. C.; Mendonça, C. R. *Adv. Mater.* **2005**, 17, 1890–1893.
- (60) Kogej, T.; Beljonne, D.; Meyers, F.; Perry, J. W.; Marder, S. R.; Bredas, J. L. *Chem. Phys. Lett.* **1998**, 298, 1–6.
- (61) Beljonne, D.; Wenseleers, W.; Zojer, E.; Shuai, Z.; Vogel, H.; Pond, S. J. K.; Perry, J. W.; Marder, S. R.; Brédas, J. L. *Adv. Funct. Mater.* **2002**, 12, 631.
- (62) Martineau, C.; Lemerrier, G.; Andraud, C.; Wang, I.; Bouriau, M.; Baldeck, P. L. *Synth. Met.* **2003**, 138, 353–356.
- (63) Pruzinsky, S. A.; Braun, V. *Adv. Funct. Mater.* **2005**, 15, 1995–2004.
- (64) Drobizhev, M.; Stepanenko, Y.; Dzenis, Y.; Karotki, A.; Rebane, A.; Taylor, P. N.; Anderson, H. L. *J. Am. Chem. Soc.* **2004**, 126, 15352–15353.
- (65) Drobizhev, M.; Karotki, A.; Kruk, M.; Mamardashvili, M. Z.; Rebane, A. *Chem. Phys. Lett.* **2002**, 361, 504–512.
- (66) Drobizhev, M.; Karotki, A.; Kruk, M.; Rebane, A. *Chem. Phys. Lett.* **2002**, 355, 175–182.
- (67) Belfield, K. D.; Corredor, C. C.; Morales, A. R.; Dessources, M. A.; Hernandez, F. E. *J. Fluoresc.* **2006**, 16, 105–110.
- (68) Yates, S. F.; Schuster, G. B. *J. Org. Chem.* **2002**, 49, 3349–3356.